Journal of
Synchrotron Radiation

ISSN 0909-0495

Received 12 February 2007
Accepted 21 May 2007

ID20: a beamline for magnetic and resonant X-ray scattering investigations under extreme conditions

L. Paolasini,* C. Detlefs, C. Mazzoli, S. Wilkins,‡ P. P. Deen,¶ A. Bombardi,§ N. Kernavanois, F. de Bergevin, F. Yakhou, J. P. Valade, I. Breslavetz,‡‡ A. Fondacaro, G. Pepellin and P. Bernard

European Synchrotron Radiation Facility, BP 220, 38043 Grenoble, France. E-mail: paolasin@esrf.fr

A new experimental station at ESRF beamline ID20 is presented which allows magnetic and resonant X-ray scattering experiments in the energy range 3–25 keV to be performed under extreme conditions. High magnetic field up to 10 T, high pressure up to 30 kbar combined with low temperatures down to 1.5 K are available and experiments can be performed at the *M*-edges of actinide elements, *L*-edges of lanthanides and *K*-edges of transition metals.

Keywords: resonant X-ray magnetic scattering; high magnetic fields; high pressure; strongly correlated electron systems.

1. Introduction

The research field of resonant X-ray scattering (RXS) has experienced tremendous theoretical and experimental progress during recent years, and today it is one of the most important areas of investigation of modern synchrotron radiation sources (Gibbs *et al.*, 2002). This method uses the photon beam as a quantum probe to investigate structural, magnetic and electronic ordered structures of solids. It represents a meeting point between the theoretical understanding of photon interaction with bound electrons in condensed matter and the exploitation of the main characteristics of a third-generation synchrotron beam: light polarization control and analysis (linear and circular), fine energy tuning, focusing, high flux and beam stability. The ID20 magnetic scattering beamline at the European Synchrotron Radiation Facility (ESRF) was one of the first instruments built at a third-generation synchrotron radiation source specifically to carry out studies on magnetic systems (Stunault *et al.*, 1998). Its successful operation relies on a combination of the main features of the ESRF beam with a sophisticated and specialized experimental set-up, which include versatile scattering geometries and dedicated sample environments adapted for RXS studies.

RXS combines high-Q resolution X-ray diffraction with atomic spectroscopy for investigating the subtleties of microscopic electronic and magnetic interactions in systems where the ground-state properties reflect a delicate balance between several different electronic competing processes. The fundamental interaction of X-rays with bound electrons can be due to the electron charge or by the coupling between the electric and magnetic field of the incident photons with the atomic magnetic moment. Charge scattering is the dominant mechanism and the basis for crystallographic investigation of condensed matter. X-ray magnetic scattering gives rise to two regimes that are determined by the incident photon energy: the non-resonant limit, in which the incident X-ray energy is well separated from the excitation energy of any atomic absorption edge in the solid, and the RXS regime, where the incident X-ray energy lies near an absorption edge. The large X-ray detection range, which spans from the weak non-resonant magnetic intensity (comparable with the resonant magnetic enhancement at the *K*-edge of transition metals) to the large enhancement *M*-edges of the actinides, of the same order of magnitude as the Thomson scattering, requires high photon flux such as delivered by undulator beamlines at third-generation synchrotron radiation sources.

In the resonant regime, when the incident X-ray energy is tuned across an absorption edge, there are additional contributions to the X-ray scattering cross section. The fundamental idea of RXS is that the incident photon energy is sufficient to cause a core-level electron to be injected into a partially filled valence band shell and subsequently decay through the emission of an elastically scattered photon with particular polarization dependence. The special nature of this process is that it is both electron-shell and element specific, and it has introduced species sensitivity directly into the determination of magnetic structures (Hannon *et al.*, 1988; Blume, 1994).

Compelling scientific problems in contemporary condensed matter physics and material science make the development of extreme sample environment conditions necessary to achieve major scientific breakthroughs. The application of external degrees of freedom such as low temperature (T), high pressure (P) and high magnetic field (H) combined with the RXS

‡ Present address: BNL, Upton, NY 11973-5000, USA.
¶ Present address: ILL, BP 220, 38042 Grenoble, France.
§ Present address: Diamond Light Source Ltd, RAL, Chilton, Didcot OX11 0QX, UK.
‡‡ Present address: GHMFL, CNRS, BP 166, 38042 Grenoble, France.

technique are important tools for investigating electronic and magnetic quantum phase transitions in strongly correlated electron systems. With this motivation, the main beamline refurbishment project which has been undertaken during the last five years concerns the construction of a new experimental hutch (EH2) which accommodates a dedicated six-circle (SIXC) diffractometer to support heavy loads and a superconducting split-pair magnet of 10 T adapted to the RXS studies. The new facility, commissioned during Autumn 2005, is today available for user experiments when horizontal scattering geometry and heavy sample environment equipment are required (cryostats, magnets, high-pressure cells), whereas the first experimental hutch EH1 is dedicated to the azimuthal studies of photon polarization in the vertical scattering geometry.

This paper describes the scientific and technical accomplishments of the ID20 beamline during the past few years of operation and summarizes the available instrumentation and experimental set-ups.

2. Front-end and optics layout

The ID20 beamline is a UHV beamline, built on a high-β straight section, thus with a relatively large source size (818 µm horizontally and 23.5 µm vertically) and a very small divergence (15 µrad). Today, ID20 receives radiation from three linear undulators (length 1.6 m and maximum field of 0.7 T), two u35 and one u32 (35 mm and 32 mm period, respectively), with a brilliance of the order of 10^{20} photons s^{-1} (0.1% bandwidth)$^{-1}$ mm^{-2} mrad^{-2} at 200 mA. The choice of the period was made taking into account the small gap obtainable with the new in-vacuum chambers of 10 mm, and the positioning of the first harmonic at the smallest working energy, which correspond to the U M_5-edge, E = 3.552 keV. The upper limit, in principle, can be set at around 20–25 keV, and experiments above 15 keV (*i.e.* at the L-edge of transuranium elements) are not very common at ID20. At 7.5 keV (Tb L_3-edge, E = 7.514 keV) it is necessary to change the first harmonic of u32 with the third harmonic of u35. With the present insertion devices, the flux available at the sample ranges from $\sim 10^{13}$ photons s^{-1} at 4 keV up to $\sim 10^{14}$ photons s^{-1} at 10 keV at 200 mA when two undulators are closed at the minimum gap (11 mm). The general layout of the ID20 optics hutch, represented in Fig. 1, consists of a double-crystal Si(111) monochromator embedded between two focusing mirrors in a vertical scattering geometry, mounted on a rigid girder (Stunault *et al.*, 1998).

The optics system is separated from the storage-ring vacuum only by differential pumping (5×10^{-9} mbar) and each optic element has its own ionic pumping system. The vacuum performances are very good, with a base pressure in the 10^{-9} mbar range without the beam and not exceeding 1×10^{-8} mbar with the full beam. Only a Be window (thickness 500 µm) separates the optics hutch from the experimental hutch; the UHV section terminates at the entrance of the experimental hutch EH1 with a second Be window which can be removed, the vacuum being assured by an additional differential pumping system.

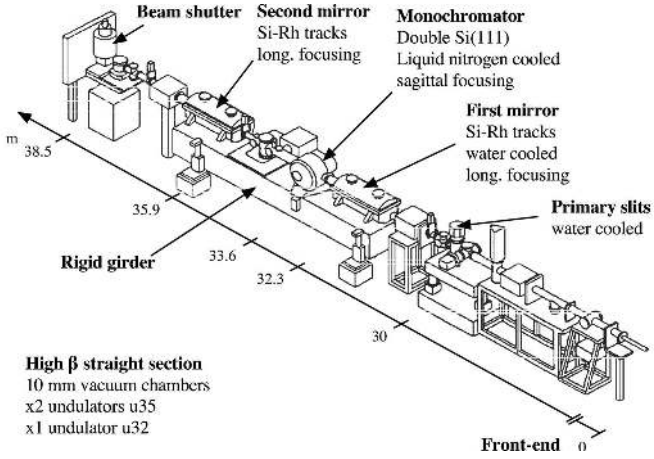

Figure 1
Viewgraph of the ID20 optics hutch.

2.1. Monochromator

The ID20 monochromator consists of a Si(111) double crystal; the first crystal is cooled by liquid nitrogen and the second crystal is mounted on a bender for a tunable sagittal focusing. The monochromator vacuum chamber can be rotated about an axis parallel to the scattering plane, in order to avoid glitches owing to multiple Bragg diffraction produced in the monochromator crystal (anti-glitch system). A fine rotation of the two-crystal assembly (accuracy of ± 0.6 arcsec, reproducibility of ± 0.4 arcsec = 1 eV at 9 keV), allows measurements between 3.4 and 25 keV, with a resolution of about 8 eV at 9 keV (Stunault *et al.*, 1998).

2.2. Mirrors

The double mirrors were designed for high-order harmonic rejection and to provide vertical focusing over a wide energy range (3.5–25 keV). Both are made from 1 m-long silicon ingots (70 mm × 50 mm × 1000 mm) and contain two different reflecting surfaces (pure silicon and a 600 Å-thick rhodium coating), which can be changed by translating the mirror assembly (translation limited to ± 30 mm by mechanical constrains). The working range of the mirror angles for harmonic rejection is between 2 and 8 mrad. Above 12 keV the rhodium track is used.

Four independent mechanical actuators bend the mirrors from the corners. Strain gauge load cells positioned directly on the actuators give a direct measurement of the actual pressure corresponding to the bending moment. The first mirror receives all the heating power of the undulator beam ($\sim$300 W). The second mirror, similar to the first one, provides the vertical focusing into the experimental hutches. The radii of curvature are in the range 0.8–30 km with a slope error of ± 2 µrad.

The installation of the new Huber six-circle diffractometer (6.8 m downstream of the first diffractometer in EH1) requires a second focal point, which decreases the demagnification

factor from 2.5 for EH1 to 1.7 for EH2. Typical focused spot sizes at the sample positions are ~250 μm (V) and ~300 μm (H) for EH1 and ~400 μm (V) and ~500 μm (H) for EH2. We notice that the horizontal focusing is close to the theoretical calculation based on the divergence and the spot size of the source. The vertical focusing is affected by the slope error on the two mirrors and can be calculated by the expression $2\sqrt{2}\Delta S_e d$, where d is the distance between the mirror and the focal spots, $\Delta S_e = 4$ μrad is the slope spread on one mirror, the factor $2\sqrt{2}$ is due to two mirrors in sequence and the deviation of the X-ray beam from 2θ.

Upgrade of the optics hutch elements is planned in the next years, and the design studies include high-power heat load on the optic elements owing to the front-end upgrading, the improvement of the beam stability and the focusing performances in both the experimental hutches.

3. Experimental methods and set-ups

In the RXS technique the choice of the scattering geometry and the sample environment is strictly related to the complex relationships between the photon polarization state and the scattering wavevector **Q** with respect to the sample orientation. The RXS method consists of measuring the enhancement of the scattering intensities when the incident photon energy is tuned close to an absorption edge of a given chemical element in a material. This method reveals static correlations, as in the case of standard X-ray diffraction methods, and provides information on the local site symmetry of the electronic shells, as in the case of spectroscopy experiments (Vettier, 2001).

A feature of the resonant enhancement is the tensor character of atomic structure factors near the absorption edge which reflect the anisotropy of the electronic shells: low site symmetry, Jahn–Teller distortion, local magnetization or electronic orbital order. Owing to the tensor character of the atomic structure factor, superlattice diffraction peaks, forbidden by the space-group symmetries, would appear to be originating from the occurrence of the long-range ordering of any physical quantity coupled with the electronic density of states. Similar to other near-edge photon absorption spectroscopies, the light polarization is strongly influenced by small changes in the local site electronic symmetries, and the analysis of the scattered photon polarization as a function of the incident energy and the sample orientation is the method used to unravel the physics that is at the origin of the resonant signals.

Table 1 shows the absorption edges exploited for RXS studies and associated with the elements of interest for magnetic diffraction. The rows in italic represent absorption edges in the soft X-ray regime, where the scattering conditions are not fulfilled for most of the ordered magnetic structures, but with a huge enhancement of the resonant magnetic amplitude, as shown in the last column (L-edges of transition metals and M-edges of rare-earths). The most important edges for hard RXS cover the energy range 3.5–15 keV, which include K-edges of transition metals, L-edges of rare-earths and both the L-edges and the M-edges of actinides. Two possible photoelectron transitions are considered in RXS: the electric dipole (E1) and the electric quadrupole (E2), which are related to the symmetry of the electronic shell and to the type of orbital probed in the intermediate states. The last column of Table 1 shows an estimation of the magnetic scattering amplitude for the different shells (Vettier, 2001).

Table 1
The photoabsorption edges for different magnetic series of elements, with the characteristic energy ranges (keV), wavelength λ (Å) and the allowed atomic transitions to the electronic shells.

The right-hand column indicates the estimated amplitude of resonant magnetic scattering expressed in r_0 units. The rows in italic represent absorption edges in the soft X-ray regime (see text).

Series	Edge	Energy (keV)	λ (Å)	Shells	Type	Magnitude
3d	$L_{2,3}$	*0.4–1.0*	*12–30*	$2p \rightarrow 3d$	*E1*	*~1.00*
	K	4.5–9.5	1.3–2.7	$1s \rightarrow 4p$	E1	~0.02
				$1s \rightarrow 3d$	E2	~0.01
5d	$L_{2,3}$	5.4–14	0.9–2.2	$2p \rightarrow 5d$	E1	~1.00
4f	$L_{2,3}$	5.7–10.3	1.2–2.2	$2p \rightarrow 5d$	E1	~0.10
				$2p \rightarrow 4f$	E2	~0.05
	$M_{4,5}$	*0.9–1.6*	*7.7–13.8*	$2d \rightarrow 4f$	*E1*	*~100*
5f	$L_{2,3}$	17–21	0.6–0.7	$2p \rightarrow 6d$	E1	~0.05
				$2p \rightarrow 4f$	E2	~0.01
	$M_{4,5}$	3.5–4.5	2.7–6	$3d \rightarrow 5f$	E1	~10.0

Because the X-ray absorption becomes large at low energy, RXS experiments probe a small scattering volume near the surface of the sample. This can be an advantage for single magnetic domain studies, but a severe limitation is introduced in the geometrical scattering condition, owing to the reduced Ewald sphere which can be probed at low energies.

3.1. Diffractometers and scattering geometries

Working under diffraction conditions and at low energies requires a necessary versatility of the sample environment equipment in terms of a wide scattering aperture and low absorbing windows.

Two experimental hutches are available at ID20 and they are designed to perform two classes of experiments: azimuthal studies by photon polarimetry (EH1) and experiments under extreme conditions (EH2) requiring heavy cryogenic devices (see Fig. 2).

EH1 contains all the necessary equipment for light conditioning and monitoring, and a 12-circle MicroControle diffractometer, designed originally to fulfill multipurpose requirements. Today it is mainly used in vertical scattering geometry (FOURC) and an extra azimuthal arm (super-φ) was developed to add a degree of freedom to the Eulerian mounting (see Fig. 3) and to perform the rotation ψ of the sample around the scattering vector **Q**. Within this configuration it is possible to measure off-specular reflections up to $\pm 20^\circ$ from the sample normal. An implemented macro allows the crystal UB matrix determination as a function of ψ and thus a rapid calculation of the desired motor positions. This set-up has provided very good scientific data and has stimulated deeper experimental investigations of the tensor character of multipole resonant amplitudes in a large number of experiments.

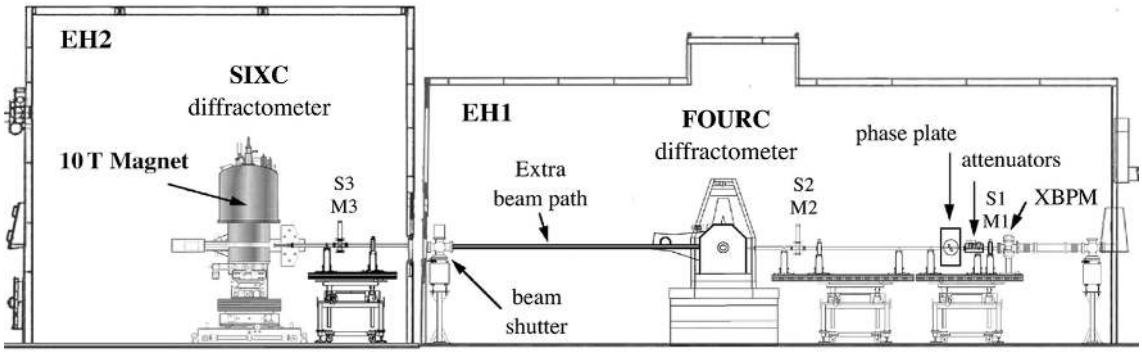

Figure 2
Schematic layout of the ID20 experimental hutches with the vertical FOURC MicroControle diffractometer (EH1) and the SIXC Huber diffractometer for high-magnetic-field studies (EH2). XBPM = X-ray beam-position monitor.

In particular, the capability of this geometry to discriminate the multiple-scattering events or to establish the magnetic domain populations make this set-up the main instrument of investigation of the RXS technique.

EH2 is large and accommodates a Huber six-circle diffractometer, designed to support a superconducting split-pair magnet or equivalent heavy load equipment (see Fig. 4). The *x*-*y*-*z* translation stages are built with non-magnetic materials. The robust detector arm is able to carry up to 25 kg with a sphere of confusion of $\sim$100 µm. As well as the standard SIXC geometries this diffractometer can be easily adapted to a wide variety of experimental geometries requiring heavy equipment such as cryostats or vacuum chambers for *in situ* film grow. Indeed, the detector arm can be used in the standard horizontal geometry or with the normal beam geometry as in the case of the 10 T magnet. Recently, the set-up used for coherence experiments was adapted to the new hutch. A set of high-precision slits with cylindrical blades are placed in the proximity of the sample (120–150 mm) and connected to a rigid support (typical opening 20 µm × 20 µm). A set of slits located at about 8 m before the sample are used as a virtual source. A long arm (2.5 m) supports an in-vacuum flight path, a CDD camera (20 µm × 20 µm pixel size) and a set of supports for APD (avalanche photodiode) detectors and slits for sample alignment. This arm is equilibrated by the diffractometer arm load and can be used in all of the three-dimensional spatial directions.

3.2. Polarization analysis

The azimuthal dependence and polarization analysis is a method which directly measures the symmetries of the tensors

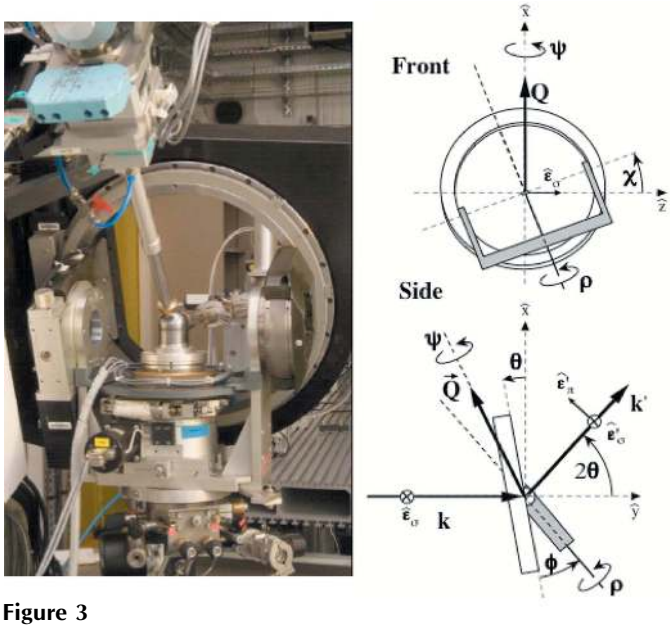

Figure 3
Left: azimuthal set-up mounted on the Φ circle of the MicroControle diffractometer. Right: drawing of the azimuth sample rotation stage which allows the full rotation of the Displex around its axis ρ. ψ is the azimuthal angle around the scattering vector **Q**. The incident light polarization $\hat{\varepsilon}_\sigma$ is perpendicular to the vertical scattering plane defined by the incident and scattered photon wavevectors **k** and **k**′, respectively.

Figure 4
General view of the experimental hutch EH2 with the ^{4}He evaporation cryostat mounted on the Huber six-circle diffractometer.

Table 2
Crystal analyzers available at ID20 for triple-axis configuration.

Crystal	(*H K L*)	*d* (Å)
Ge	(1 1 1)	3.266
Ge	(2 2 0)	2.001
Si	(1 1 1)	3.135
Si	(2 2 0)	1.920
Si	(4 0 0)	1.358

involved in resonant scattering amplitudes by measuring the diffracted X-ray linear polarization upon rotating the sample around the scattering vector. Fig. 5 shows a typical set-up for an RXS experiment. The use of a polarization analyzer (PA) accounts for different functions, achieved by a Bragg diffraction with an analyzer crystal (AnC): (i) increasing the 2θ angular resolution; (ii) reducing the fluorescence background near the absorption edges; (iii) selecting the polarization of the sample diffracted beam ($\mathbf{k}'$).

The AnC is installed in the PA and set to a normal to the surface Bragg diffraction fulfilling the elastic condition $|\mathbf{k}| = |\mathbf{k}''|$. This prevents sample fluorescence and other spurious signals coming from the sample environment from entering the detection chain, located at the PA exit.

For high-Q resolution studies, for example to resolve very small lattice distortions in the sample, very high quality single crystals are needed with high reflectivity and narrow rocking curve to enhance as much as possible the resolution by limiting the angular acceptance.

Table 2 shows a list of crystals available at the ID20 beamline to work in the triple-axis configuration. In this case the θ_p AnC Bragg angle is kept rather small so that the polarization of the signal is almost not affected and the whole elastic signal can be detected.

The polarization detection is realised by choosing a suitable crystal, fulfilling the diffraction condition $\theta_p \simeq 45^\circ$ at the current energy. This fact limits the use of each crystal to a narrow energy band so that a complete collection of AnC is

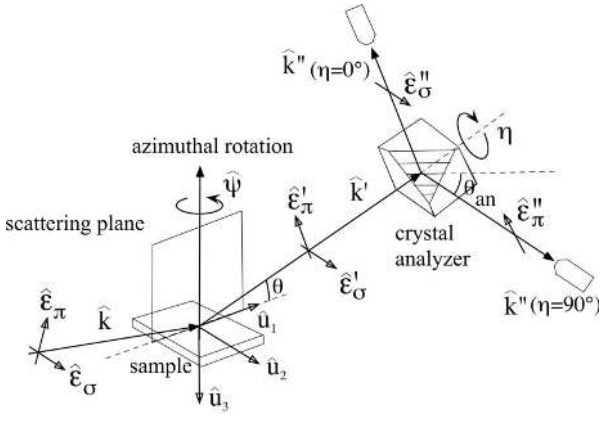

Figure 5
Description of the vertical scattering geometry with the polarization analysis set-up. A crystal analyzer is selected and oriented for a given energy with a Bragg scattering angle $\theta_{an} \simeq 45^\circ$, and it can be rotated about the scattered wavevector $\mathbf{k}'$ (angle η). For scattered photons with polarization $\hat{\varepsilon}'_\sigma$ ($\hat{\varepsilon}'_\pi$), the intensity is detected when $\eta = 0^\circ$ ($\eta = 90^\circ$).

Table 3
Crystals available at ID20 for polarization analysis.

Crystal	(*H K L*)	*d* (Å)	*E*(90°) (keV)
Graphite	(0 0 2)	3.35440	2.612
Ge	(1 1 1)	3.26600	2.682
Si	(1 1 1)	3.135	2.797
Au	(1 1 1)	2.35454	3.721
Al	(1 1 1)	2.33827	3.747
Al	(2 0 0)	2.02500	4.326
Ge	(2 2 0)	2.001	4.381
Si	(2 2 0)	1.920	4.566
Graphite	(0 0 4)	1.67720	5.223
Mo	(2 0 0)	1.5739	5.571
β-Brass	(2 0 0)	1.477	5.9357
Al	(2 2 0)	1.43189	6.118
LiF	(2 2 0)	1.42376	6.153
Ge	(4 0 0)	1.415	6.196
Al_2O_3	(0 3 0)	1.37400	6.376
Si	(4 0 0)	1.358	6.458
Cu	(2 2 0)	1.27633	6.864
InSb	(3 3 3)	1.24708	7.025
MgO	(2 2 2)	1.21567	7.206
β-Brass	(2 1 1)	1.206	7.2695
Mo	(2 2 0)	1.1133	7.876
Ge	(3 3 3)	1.08866	8.047
Si	(3 3 3)	1.045	8.390
β-Brass	(2 2 0)	1.044	8.3975
Cu	(2 2 2)	1.04212	8.407
LiF	(4 0 0)	1.00675	8.702
Pd	(4 0 0)	0.9743	8.9987
Au	(3 3 3)	0.78485	11.162
Si	(4 4 4)	0.784	11.182
Al	(3 3 3)	0.77942	11.240
Al	(4 4 0)	0.71590	12.237
LiF	(4 4 0)	0.71188	12.306

necessary to suitably cover the wide energy range 3–15 keV which includes the *M*-edges of actinides (3.5–5 keV), the *L*-edges of rare-earths (6–10 keV) and the *K*-edges of transition metals (5–10 keV). In Table 3 a list of currently available AnCs is reported.

To take into account the linear polarization dependence of a single scattering process we define $\hat{\varepsilon}_\sigma$ and $\hat{\varepsilon}_\pi$ as the unit vectors perpendicular and parallel to the sample diffraction plane, as sketched in Fig. 5, so that the Jones matrix for Thomson scattering at the AnC between the incident ($\hat{\varepsilon}'$) and analyzed ($\hat{\varepsilon}''$) polarizations is

$$\varepsilon'' \cdot \varepsilon' = \begin{pmatrix} \varepsilon''_\sigma \\ \varepsilon''_\pi \end{pmatrix} \begin{pmatrix} 1 & 0 \\ 0 & \cos(2\theta_p) \end{pmatrix} \begin{pmatrix} \varepsilon'_\sigma \\ \varepsilon'_\pi \end{pmatrix},$$

where 1 is the matrix element involving the $\hat{\varepsilon}'_\sigma \rightarrow \hat{\varepsilon}''_\sigma$ process, $\cos(2\theta_p)$ is that involving $\hat{\varepsilon}'_\pi \rightarrow \hat{\varepsilon}''_\pi$, and the off-diagonal elements are zeros (no polarization rotation is allowed in the case of Thomson scattering). Note that the Jones matrix given before holds for the AnC sketched in Fig. 5 because both the sample diffraction plane and that of the AnC are coincident. In fact, this is a very convenient way of defining the $\eta = 0$ position for both pure vertical and horizontal diffraction geometries (σ–σ and π–π channels, respectively).

For a general η angle position the detected intensity can be expressed as

$$I_{PA}(\eta) = I''(\eta) = \cos^2(\eta)\left|\varepsilon'_\sigma\right|^2 + \sin^2(\eta)\left|\varepsilon'_\pi\right|^2.$$

With the new analyzer it is possible to rotate the η axis through 2π, and a complete linear polarization analysis of the sample diffracted light can be obtained (Blume & Gibbs, 1988; Blume *et al.*, 1988). In reality, both experimental PA misalignments, AnC imperfections and asymmetric beam divergence require these measurements to be performed in a different way. AnC is rocked *via* a θ_p motor for a set of η values and the information on the sample diffracted polarization is then recovered by fitting the measured integrated areas with the $I_{PA}(\eta)$ function given above. In this case the characteristics needed for a good AnC are slightly different with respect to the previous case: always high reflectivity but higher acceptance (worse mosaicity). A typical value of the rocking-curve (θ_p) FWHM (full width at half-maximum) is $\sim 0.2^\circ$, well suited for performing a good polarization analysis without being bothered by problems in the crystal alignment during a polarization scan. Care has to be taken in the choice of the atomic elements constituting the crystals, in order to keep AnC fluorescence as low as possible. On ID20, two identical PAs are permanently installed, one in each experimental hutch. They are realised fully under vacuum to avoid the air absorption along the diffracted path.

3.3. Light polarization conditioning: X-ray phase plates

The incident linear light polarization delivered by the planar undulators can be changed (linear or circular) by using an X-ray phase retarder (Hirano *et al.*, 1992; Giles *et al.*, 1994, 1995). A thin single crystal of diamond is inserted into the beam upstream of the sample. When the crystal is slightly detuned from the Bragg position, the transmitted σ and π waves are phase shifted with respect to each other. Different polarizations of the transmitted beam can be selected by adjusting the phase difference and the orientation of the phase plate's scattering plane with respect to the incident polarization (horizontal). Details of the operation are described in the ID20 beamline handbook (http://www.esrf.eu/exp_facilities/ID20).

Circular polarization is obtained when the phase shift is set to $\pm\lambda/4$ (quarter-wave plate) and the scattering plane is inclined by 45°. Circular polarization is particularly useful for the study of ferromagnetic and helical magnetic structures.

Linear polarization is obtained when the phase shift is set to $\pm\lambda/2$ (half-wave plate). The plane of polarization is then rotated by twice the angle by which the scattering plane is inclined. Linear polarization with variable orientation will offer an alternative to the azimuthal dependence, especially in experimental configurations that prohibit an azimuthal rotation of the sample, *e.g.* when using the cryomagnet, or for surface diffraction, where the azimuth is coupled to the angle of incidence.

Test experiments have been carried out in both the $\lambda/2$ and $\lambda/4$ mode, for photon energies ranging from 3.7 to 9.0 keV (see Fig. 6). Circular beams with polarization in excess of 95% were produced for all working energies. Working with linear polarization, however, it would be preferable to implement a divergence-compensated set-up, as the depolarization in $\lambda/2$ mode is 16 times higher than in $\lambda/4$ mode. Unnecessary intensity losses owing to windows and air paths could be avoided by integrating the phase plate mechanics into a rough vacuum chamber (Okitsu *et al.*, 2001).

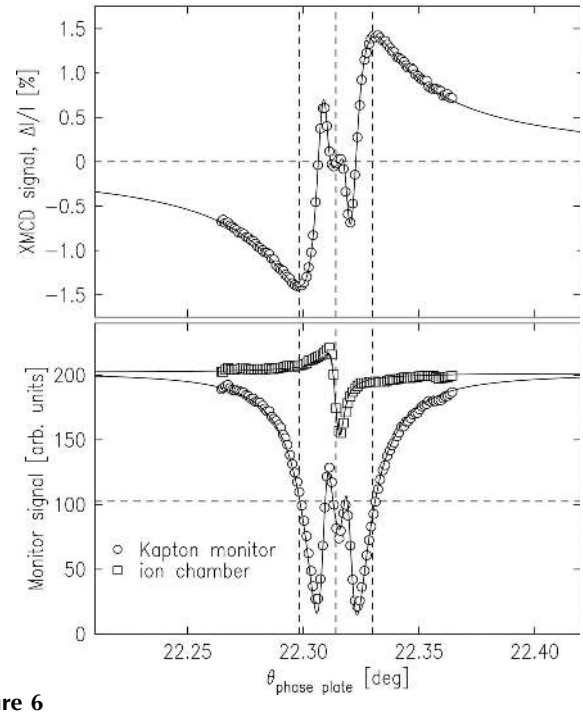

Figure 6
Calibration experiment for the X-ray phase plate. Top: X-ray magnetic circular dichroism signal at the Gd L_2-edge of a GdCo thin-film reference sample. Bottom: intensity monitored by an ionization chamber (squares) and 90° scattering of a Kapton foil (circles). Continuous lines: calculations with dynamical theory.

3.4. Detection and monitoring

In most of the ID20 experiments X-ray detection is performed by single-photon detection chains, apart from some particular set-ups like photon correlation spectroscopy experiments, which require a two-dimensional detector to rapidly acquire in one shot the spatial interference of the beam. Two kinds of detector are currently available on the beamline: photomultiplier and solid-state device silicon APD (ESRF design).

The APD detectors are orders of magnitude faster, resulting in a high dynamical range (10^7 counts are accessible); it is also more robust, being able to tolerate the direct monochromatic beam without failure. They are currently the unique available detector used for high magnetic fields; in fact, sample environment proximity strongly limits the use of sensible photomultipliers to low values of the applied magnetic field (stray field of ~ 0.03 T at 1 m for the 10 T superconducting magnet). A real drawback of the APD is the stopping power: being a thin slab of Si it starts to lose detecting efficiency (photosensitivity) at 7–8 keV. In the case of low counting rates at high energies, photomultipliers are still a valid choice as a detector, if no magnetic field is applied.

4. Sample environments

In this section we describe the instrumentation developed at ID20 which will allow further systematic studies of *H–P–T* magnetic phase transitions in the RXS regime, providing new research capabilities as well as building up expertise leading to technological advances in this technique.

4.1. Low temperatures

Low temperatures represent the main thermodynamical variable for studying magnetic systems. Our beamline extensively uses this important external degree of freedom to study the order parameters of electronic and magnetic phase transitions in materials. One of the most interesting fields of condensed matter physics concerns critical quantum effects located below 1 K: heavy fermion superconductors, quantum critical point behavior, interplay between quadrupolar ordering and magnetism, to cite a few examples. For these reasons, a large effort was undertaken during recent years to achieve the lowest temperatures compatible with the thermal heating of the photon beam. The increasing of photon flux up to 10^{13} photons s^{-1} (at 9 keV this corresponds to about 40 mW of heating power) and the strong absorption of the sample surface around the characteristic working energies affect the thermal behavior of measured materials. Indeed, sample composition (insulating, metallic, superconductive materials), thermal contacts, absorption around the characteristic edges, and incident photon flux are all important parameters to be taken into account to reach the lowest temperatures.

The prime cryogenic equipment for low temperatures is the ^{4}He evaporation cryostat (developed at ILL and called orange cryostat, see Fig. 4). It can reach the lowest temperature of 1.55 K with a cooling power of about 20 mW by forcing ^{4}He evaporation with a pumping stage on the tail. It can be mounted only in horizontal geometry, and cannot be inclined more than $\pm 5^\circ$. The absence of vibrations is the main characteristic of this system, which is the perfect device for coherence or surface experiments at very low temperature.

In 2004 we completed a project with the ILL cryogenic pool to develop a compact closed-cycle refrigerator with a ^{4}He Joule–Thomson evaporation stage on the cold head. This Displex reaches a minimal temperature of 1.8 K, is user-friendly, and can be mounted on the azimuthal stage (see Fig. 3). Despite the strong vibration induced on the sample, and the relatively small cooling power (moderate thermal heating effects), it is nowadays one of the main tools for performing azimuthal scans without geometrical restrictions. A second spare Displex reaching the standard temperature of 10 K is also available.

4.2. High-pressure set-up

The application of high pressures at low temperatures on strongly correlated electron systems leads to variations manifested in the electronic structure. By acting on the lattice parameter, hydrostatic pressure may vary the overlap of orbitals, thus altering the balance of competing magnetic and electronic interactions that are responsible for anomalous low-temperature thermodynamic and transport properties, thus playing an essential role in the elucidation of physical properties. RXS could therefore be an ideal technique to be combined with hydrostatic pressure in order to determine structural and electronic order parameters as a function of bond length (D'Astuto *et al.*, 2006).

The development of a hydrostatic pressure technique on ID20 was first undertaken by N. Kernavanois and continued by P. Deen in collaboration with D. Braithwaite of the CEA, Grenoble. The aim of the project was to develop a method to probe a phase diagram across 0–5 GPa and 1.5–300 K by RXS scattering at the *L*-edges of lanthanides and *K*-edges of transition metals, with *in situ* pressure and temperature variation (Kernavanois *et al.*, 2005). This challenging project requires the following experimental conditions:

(i) Scattering geometry: wide scattering angles and a scattering geometry restricted to the horizontal scattering plane.

(ii) Sample size: compromise between the small RXS cross sections and highest applied pressures.

(iii) Low absorption transmission: scattering through a beryllium gasket and use of a low-absorption-pressure transmitting medium.

(iv) Pressure variation and determination: direct application of the pressure at low temperature and *in situ* pressure determination.

Hydrostatic pressure is created *via* a moissanite (SiC) anvil cell allowing for the possibility of high pressure in combination with large sample volumes in an X-ray-transparent pressure cell. The pressure cell on ID20 employs bevelled anvils, 10 mm deep with a 2 mm cullet, bought from Charles and Colvart Ltd. These dimensions were specified as a compromise between sample dimension and the possibility of reaching 5 GPa. A non-magnetic pressure cell, designed at the CEA Grenoble, is fabricated from copper–beryllium owing to its high strength and hardness. Its dimensions are 30 mm in external diameter and 54 mm in height and it is compatible with a standard orange cryostat. The scattering geometry for the pressure set-up is therefore limited to horizontal scattering. The scattering geometry for the pressure set-up on ID20 is unique with respect to other high-pressure devices, since scattering occurs *via* the gasket, which is highly transparent to X-rays in the energy range exploited for RXS (Kernavanois *et al.*, 2005). The sample scattering surface is limited to 100 μm × 350 μm and there are no extra limitations in terms of the scattering angle, owing to the three-pillar design. The quality of sample cutting and surface preparation is essential to avoid disorientation or strong surface absorption.

Pressure is transmitted *via* a hydraulic press (design based on the uniaxial pressure stick by the ILL sample environment group) *via* a guiding rod onto the pressure cell (see Fig. 7), and this system is compatible with the internal bore of the standard orange cryostat and the 10 T superconducting magnet. The pressure medium most suited for this set-up is liquid nitrogen, which is loaded into a cryogenic dewar. The pressure is determined *via* the ruby fluorescence method with a fibre optic illuminating a ruby *via* the anvil cell positioned next to the

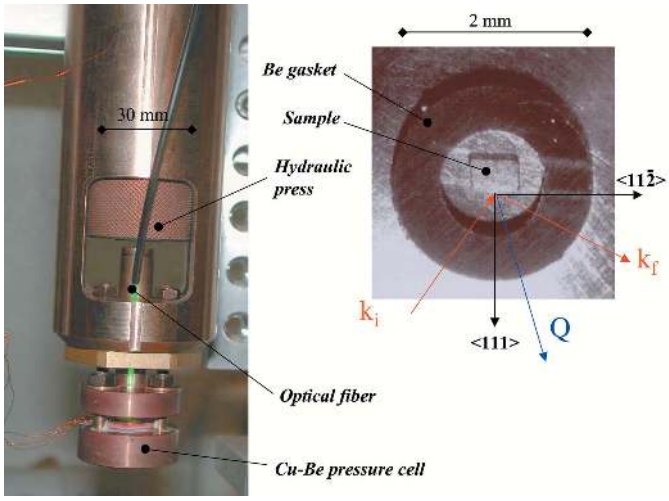

Figure 7
ID20 high-pressure set-up. Left: anvil cell with the green optical fiber for ruby luminescence detection, inserted in a solid Cu–Be block of the hydraulic press. Right: Be gasket and $Ce(Co_{0.07}Fe_{0.93})_2$ single crystal (80 μm × 200 μm × 300 μm).

sample within the gasket. The determination of pressure is possible *via* a BETSA spectrometer, thus ascertaining the pressure at all times during the experiment.

Fig. 8 shows recent experimental achievements in the detection of the small resonant magnetic signal at the Ce L_3-edge in 10% doped $CeFe_2$. These first results are encouraging and show clearly the feasibility of this technique, opening a large field of applications where low temperatures and low energies are required, as for most resonant and absorption spectroscopies (Deen *et al.*, 2005).

4.3. High-magnetic-field set-up

Magnetic fields act directly on the exchange interactions between the magnetic elements and allow fine tuning of the delicate balance between different correlation effects. The combination of external applied magnetic field and RXS technique gives unique possibilities for investigating the complex relationships between the correlated microscopic properties of magnetic materials. Magnetic fields influence the domain formation (magnetic annealing, single magnetic domain studies), induce magnetic phase transitions (meta-magnetism, frustrated magnetism in low-dimensional magnets) and remove the degeneracy of complex magnetic structures (multi-*k* magnetic structures).

For spectroscopic applications, the field direction is generally required to be along the beam direction, and X-ray optical access over a relatively small solid angle is sufficient. For diffraction applications, a field direction perpendicular to the beam is preferred, and X-ray optical access over a wide solid angle is needed.

The ID20 beamline is currently equipped with two superconducting magnets (manufactured by Oxford Instruments Superconductivity) which can be placed in EH2 (Fig. 9). They differ in both the value and the geometry of the generated magnetic field: Oxford horizontal field magnet (OxH): 3.4 T; Oxford vertical field magnet (OxV): 10 T.

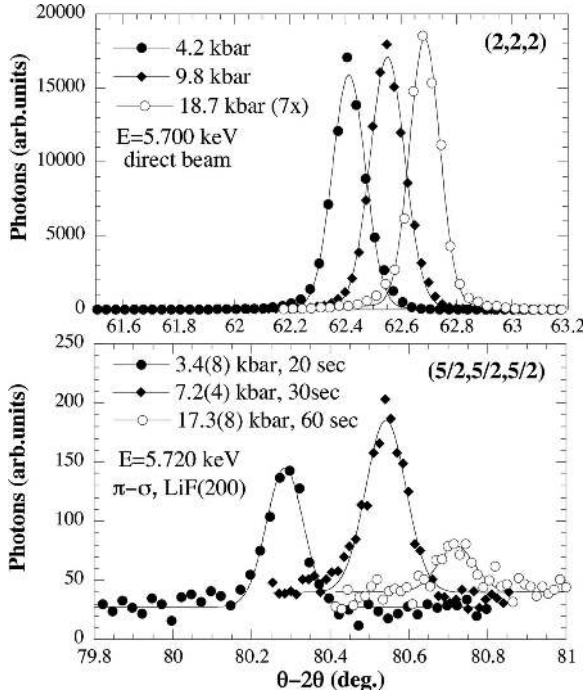

Figure 8
High-pressure experiments on $Ce(Co_{0.1}Fe_{0.9})_2$. Top: (222) Bragg reflection as a function of the pressure taken at 100 K. Bottom: antiferromagnetic reflection (5/2, 5/2, 5/2) taken at low temperatures at the Ce L_3-edge in the π–σ polarization channel (from Braithwaite *et al.*, 2006).

Figure 9
The 10 T split-coil superconducting magnet installed in EH2. All the magnet services including leads, vacuum tubes, gases and electrical connections come from the top and are connected by a pivoting vacuum arm fixed on the wall.

The OxH magnet is based on a standard Oxford magnet for spectroscopic measurements converted for use with X-ray scattering, in which the horizontal geometry is realised by two superconducting coils. As a result (see Fig. 10*a*), the position and extension of blind angles strongly limit the diffraction capabilities, while it is suitable for both transmission geometry and surface diffraction experiments.

The OxV magnet, installed on the beamline during Spring 2005, has required a special non-magnetic horizontal diffractometer capable of dealing with heavy loads (magnet weight ∼550 kg). Fig. 9 shows a typical installation of the 10 T magnet under experimental conditions in EH2. A tilting angle on the χ circle is allowed ($\pm 3^\circ$) for the magnet; nevertheless, the γ circle on the detector arm is used to collect diffraction spots falling out of the horizontal plane. As sketched in Fig. 10(*b*), the unique design split-coil pair realises a vertical field of up to 10 T with a very wide accessible angle in the horizontal plane. The restricted number of blanks and their limited angular extension mechanically limit the top value of the field. Note that their asymmetric distribution allows transmission geometry experiments to be performed as well. The homogeneity of the field is about 0.0035% over 1 mm and better than 0.1% over 5 mm in the sample zone. The measured opening angle in the vertical direction is $\pm 5^\circ$, limiting the accessibility to reflections out of the horizontal plane.

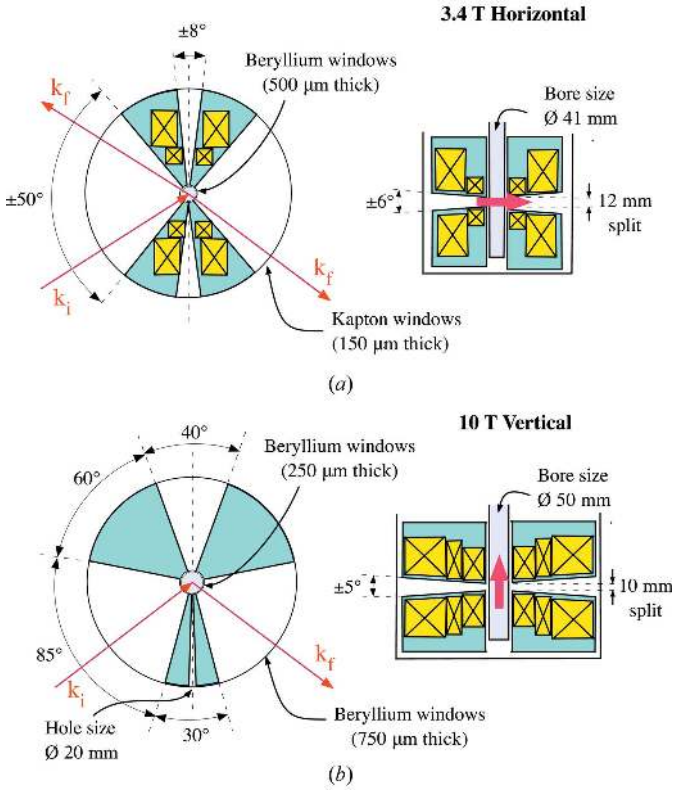

Figure 10
Top (left) and side (right) views of the ID20 superconducting magnets, showing the opening angles for X-ray access. Blind zones are marked in light blue, the red arrows indicate the incident and scattered wavevectors for different possible scattering geometries, and the thick pink arrow indicates the direction of the applied magnetic field.

The magnet cold bore has an internal diameter of 50 mm at the sample space, allowing a very large sample stick to be accommodated (*e.g.* a diamond-anvil cell for high pressure or complex *in situ* cross techniques). The cryogenic liquid fillings (nitrogen and helium) are the unique manual operations left: typically for the OxV magnet, a helium charge (internal dewar volume ∼35 L) lasts for one to two days while the nitrogen charge (∼45 L) lasts for two to three days.

Fig. 11 shows RMXS measurements on two single crystals of Co-doped $CeFe_2$ using the 10 T magnet. The data are also compared with previous neutron scattering data for the 7% Co-doped compound, sensitive to the Fe magnetic moment (Paolasini & Lander, 2000). The chemical selectivity of RMXS at the Ce L_3-edge allows in this case the determination of the Ce sublattice magnetization. Moreover, thanks to the high-Q resolution and the single magnetic domain sensitivity of the X-rays probe it was possible to elucidate the nature of the low-temperature behavior found with previous bulk-sensitive neutron scattering (Paolasini *et al.*, 2007).

Both magnets are equipped with a variable-temperature insert (VTI) standard Oxford cryostat, capable of a 2–300 K temperature range at the sample. The cooling power is obtained by spilling part of the liquid He from the main magnet reservoir and evaporating it in the exchanger zone (solid Cu block) under pumping. The temperature is controlled in two ways: roughly, through a motorized needle valve upstream of the exchanger which limits the amount of available liquid He, and finely, *via* an electric heater directly dipped into the exchanger. In both the VTIs the sample space is realised as a separated chamber filled with exchange gas and in thermal contact with the exchanger. A pressure gauge permanently controls the sample space to avoid air contamination.

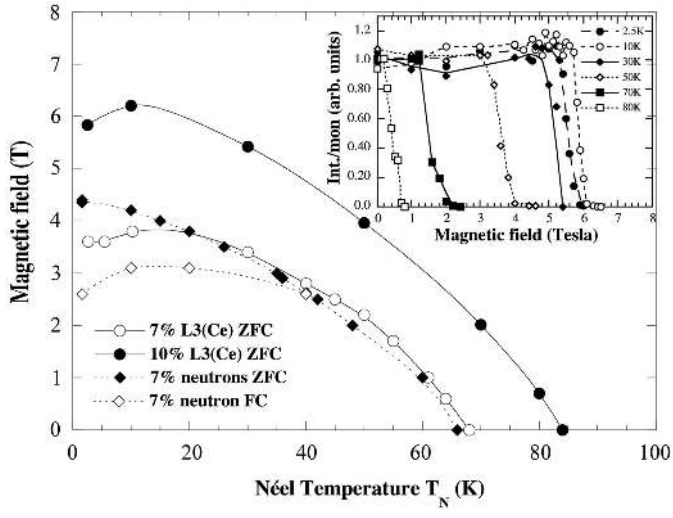

Figure 11
Magnetic phase diagram determined for the 10% (closed circles) and 7% (open circles) Co-doped samples. The neutron data for the 7% doped sample (diamonds) are taken from Paolasini & Lander (2000). The inset shows the zero-field cooling RMXS intensities as a function of the magnetic field at different temperatures for the 10% Co-doped sample.

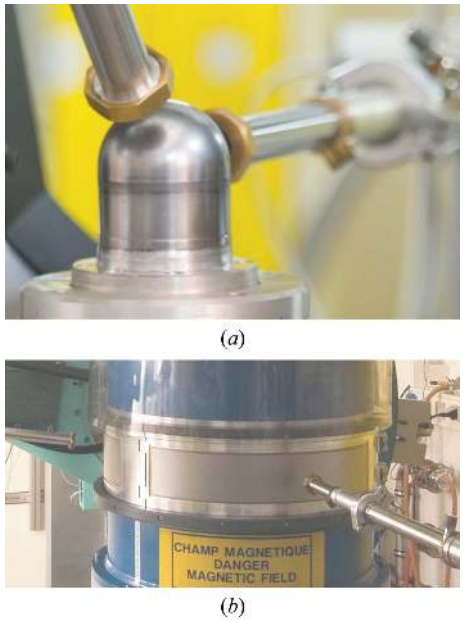

(*a*)

(*b*)

Figure 12
(*a*) External beryllium dome (500 µm) for the low-temperature azimuthal displex. (*b*) External Be windows of the OxV of thickness 750 µm. The internal VTI insert has an extra Be window of thickness 250 µm (made by BrushWellman).

4.4. Beryllium windows and in-vacuum flight paths

Particular attention is given to the low absorption conditions necessary to perform RXS in the energy range 3–8 keV. Beryllium windows are widely used on ID20 on most of the cryogenic systems rather than the usual Kapton windows.

The high photon density at the entrance of the cryogenic equipment prevents the use of Kapton because it burns very rapidly with consequences on the vacuum performances or implosion of the cryostat itself. Three special Be domes have been designed for the low-temperature Displex, with a spherical shape, and with different thickness for sample exchange gas (250 µm), thermal radiation screen (250 µm) and external vacuum insulation (500 µm) (Fig. 12*a*).

The orange cryostat and the 10 T cryomagnet are both provided with an internal (250 µm) and an external annular Be window (500 µm for the orange cryostat and 750 µm for the 10 T magnet, as shown in Fig. 12). The internal thermal screens are made from aluminized Mylar. All the incident and diffracted monochromatic beam flight paths are under vacuum (10^{-2} mbar) and they are provided with telescopic elements to reduce the air gaps as much as possible.

5. Scientific applications

The core activity of the beamline consists of measuring, close to the absorption edge, the diffracted intensity of forbidden lattice reflections appearing as a consequence of broken lattice symmetries (magnetic, charge or multipolar), and characterizing them in terms of light polarization, angular dependence about the scattering vector (azimuthal dependence), and energy dependence across the absorption edge. The shell and the chemical selectivity of the RXS technique allows the 3*d* and the 4*p* shells of transition metals (*K*-edge), the 4*f* or the 5*d* shells of lanthanides (*L*-edges), and the 6*d* or the 5*f* shells of actinides (*L*- and *M*-edges) to be probed directly. The azimuthal dependence is a method which directly measures the symmetries of the tensors involved in resonant scattering amplitudes by measuring the diffracted X-ray linear polarization upon rotating the sample around the scattering vector. This technique has been essential in a number of high-profile cases, as for example the orbital ordering in transition metals (Paolasini *et al.*, 1999; Caciuffo *et al.*, 2002; Subias *et al.*, 2006), charge ordering and metal–insulator transitions (Staub *et al.*, 2002; Scagnoli *et al.*, 2005), frustrated magnetism in low-dimensional systems (Bombardi *et al.*, 2004) or induced magnetism in non-magnetic elements (Mannix *et al.*, 2001). The azimuthal dependence can also be used to discriminate the magnetic domain populations in the non-resonant magnetic X-ray scattering regime, in order to determine the ratio between the ordered orbital and spin magnetic moment as well as their reciprocal directions (Neubeck *et al.*, 2001; Langridge *et al.*, 1997; Stunault *et al.*, 2004). Interesting physics can also be addressed in multi-*k* antiferromagnets (Longfield *et al.*, 2002; Bernhoeft *et al.*, 2004) in which quadrupolar and magneto-vibrational interactions are far from negligible.

During the last years, the possibility to single out structural, magnetic and anomalous scattering components through Bragg diffraction, and to study the polarization dependence of the diffracted beam as a function of scattering angles and incident photon energy has provided a large amount of experimental data, which in turn have stimulated theoretical calculations and interpretations. In particular, the separation of the signal in terms of electromagnetic multipoles is, at present, one of the most fashionable ways to classify these experiments and opens new avenues in this research field (Marri & Carra, 2004; Di Matteo *et al.*, 2005). The knowledge of electric and magnetic multipoles of both parities under space-inversion and time-reversal can be of great importance in order to understand the physics of strongly correlated electron systems and their investigation has been a common theme of research during the last 20 years. In the light of this interpretation, the RXS technique can be applied to the investigation of many complex materials, such as Mott insulators, colossal magnetoresistive materials, actinides, high-T_c superconductors, multiferroics, heavy fermions and other transition metal oxides, in which orbital or multipolar hidden-order parameters coexist and influence the phase transitions (Paixão *et al.*, 2002; Wilkins *et al.*, 2004, 2006; Walker *et al.*, 2006; Lovesey *et al.*, 2007).

The possibility to control the incident beam polarization by diamond phase plates and to analyze the polarization of the scattered photons as a function of the azimuthal scattering geometry and the incident energy will play an important role in the future of this technique, providing a way to obtain information on the symmetry of the ordered structure when several multipole excitations close in energy contribute to the same transition (Mazzoli *et al.*, 2007). Future plans of development concern the design of a dedicated diffractometer with a vertical scattering geometry for azimuthal scans, combined

with a ^{4}He flux cryostat and high cooling power (40 mW at a base temperature of 1.5 K).

Although specialized and optimized for near-edge resonant magnetic diffraction studies, ID20 has a broad range of capabilities for different scientific application in the physics of condensed matter. Examples of studies of surface magnetism (Barbier *et al.*, 2004), of magnetic thin films and heterostructures (Goff *et al.*, 2001; Kravtsov *et al.*, 2004), and of local dynamical fluctuations by photon correlation spectroscopy (Nelson *et al.*, 2002; Francoual *et al.*, 2003; Le Bolloc'h *et al.*, 2005) benefit from the experimental set-up described above. High magnetic fields, pressures and low temperatures are fundamental parameters for studying complex phase transitions and for disentangling competing electronic interactions in advanced materials. The development of extreme conditions in RXS will provide new powerful tools for investigating quantum phase transitions and the peculiar electronic behavior of strongly correlated electron systems. Strong multipolar interactions can lead to exotic states such as quadrupole-fluctuations-mediated superconductivity, or novel heavy fermion states when quadrupolar order is suppressed by an external magnetic field. Indeed, the fragile equilibrium between competing electronic interactions can be altered by applying pressure, or a sufficiently strong external magnetic field at very low temperature (below 1 K), when the thermal fluctuations are reduced compared with the quantum fluctuations. The observation and characterization in terms of ordering of discrete multipoles today places ID20 at the forefront of basic research on magnetism, and the availability of RXS extreme conditions is important for progress to be achieved.

References

d'Astuto, M., Baudelet, F., Rueff, J. P., Barla, A., Rueffer, R., Kernavanois, N. & Paolasini, L. (2006). *Lect. Notes Phys.* **697**, 375–399.

Barbier, M. R., Mocuta, C., Neubeck, W., Mulazzi, M., Yakhou, F., Chesnel, K., Sollier, A., Vettier, C. & de Bergevin, F. (2004). *Phys. Rev. Lett.* **93**, 257208.

Bernhoeft, N., Paixão, J. A., Detlefs, C., Wilkins, S. B., Javorsky, P., Blackburne, E. & Lander, G. H. (2004). *Phys. Rev. B*, **69**, 174415.

Blume, M. (1994). *Resonant Anomalous X-ray Scattering*, edited by G. Materlik, J. Sparks and K. Fisher, pp. 495–512. Amsterdam: Elsevier Science.

Blume, M. & Gibbs, D. (1988). *Phys. Rev. B*, **37**, 1779–1789.

Blume, M., Gibbs, D., Harshman, D. R. & McWhan, D. B. (1988). *Rev. Sci. Instrum.* **60**, 1655–1660.

Bombardi, A., Rodriguez-Carvajal, J., Di Matteo, S., de Bergevin, F., Paolasini, L., Carretta, P., Millet, P. & Caciuffo, R. (2004). *Phys. Rev. Lett.* **93**, 027202.

Braithwaite, D., Paolasini, L., Deen, P. P., Kernavanois, N., Yakhou, F., Canfield, P. & Lapertot, G. (2006). *Physica B*, **378–380**, 782–783.

Caciuffo, R., Paolasini, L., Sollier, A., Ghigna, P., Pavarini, E., van der Brink, J. & Altarelli, M. (2002). *Phys. Rev. B*, **65**, 174425.

Deen, P., Braithwaite, D., Kernavanois, N., Paolasini, L., Raymond, S., Barla, A., Lapertot, G. & Sanchez, J.-P. (2005). *Phys. Rev. B*, **71**, 245118.

Di Matteo, S., Joly, Y. & Natoli, C. R. (2005). *Phys. Rev. B*, **72**, 144406.

Francoual, S., Livet, F., De Boissieu, M., Yakhou F., Létoublon, A., Caudron, R. & Gastaldi, J. (2003). *Phys. Rev. Lett.* **91**, 225501.

Gibbs, D., Hill, J. P. & Vettier, C. (2002). *Third-Generation Hard X-ray Synchrotron Radiation Sources: Source Properties, Optics, and Experimental Techniques*, edited by D. M. Mills, pp. 267–310. New York: John Wiley and Sons.

Giles, C., Malgrange, C., Goulon, J., de Bergevin, F., Vettier, C., Dartyge, E., Fontaine, A., Giogetti, C. & Pizzini, S. (1994). *J. Appl. Cryst.* **27**, 232–240.

Giles, C., Vettier, C., de Bergevin, F., Malgrange, C., Grübel, G. & Grossi, F. (1995). *Rev. Sci. Instrum.* **66**, 1518–1521.

Goff, J. P., Sarthour, R. S., McMorrow, D. F., Yakhou, F., Vigliante, A., Gibbs, D., Ward, R. C. C. & Wells, M. R. (2001). *J. Magn. Magn. Mater.* **226–230**, 1113–1115.

Hannon, J. P., Trammel, G. T., Blume, M. & Gibbs, D. (1988). *Phys. Rev. Lett.* **61**, 1245–1248.

Hirano, K., Kanzaki, K., Mikami, M., Miura, M., Tamasaku, K., Ishikawa, T. & Kikuta, S. (1992). *J. Appl. Cryst.* **25**, 531–535.

Kernavanois, N., Deen, P., Braithwaite, D. & Paolasini, L. (2005). *Rev. Sci. Instrum.* **76**, 083909.

Kravtsov, E., Nefedov, A., Radu, F., Remhof, A., Zabel, H., Brucas, R., Hjörvarsson, B., Hoser, A. & Wilkins, S. B. (2004). *Phys. Rev. B*, **70**, 054425.

Langridge, S. L., Lander, G. H., Bernhoeft, N., Stunault, A., Vettier, C., Grübel, G., Sutter, C., de Bergevin, F., Nuttall, W. J., Stirling, W. G., Mattenberger, K. & Vogt, O. (1997). *Phys. Rev. B*, **55**, 6392–6398.

Le Bolloc'h, D., Ravi, S., Dumas, J., Marcus, J., Livet, F., Detlefs, C., Yakhou, F. & Paolasini, L. (2005). *Phys. Rev. Lett.* **95**, 116401.

Longfield, M. J., Paixão, J. A., Bernhoeft, N. & Lander, G. H. (2002). *Phys. Rev. B*, **66**, 054417.

Lovesey, S., Fernandez-Rodriguez, J., Blanco, J. A., Sivia, D. S., Knight, K. S. & Paolasini, L. (2007). *Phys. Rev. B*, **75**, 014409.

Mannix, D., Stunault, A., Bernhoeft, N., Paolasini, L., Lander, G. H., Vettier, C., de Bergevin, F., Kaczorowski, D. & Czopnik, A. (2001). *Phys. Rev. Lett.* **86**, 4128–4131.

Marri, I. & Carra, P. (2004). *Phys. Rev. B*, **69**, 113101.

Mazzoli, C., Wilkins, S. B., Di Matteo, S., Detlefs, B., Detlefs, C., Scagnoli, V., Paolasini, L. & Ghigna, P. (2007). *Phys. Rev. Lett.* Submitted.

Nelson, C. S., Hill, J. P., Gibbs, D., Yakhou, F., Livet, F., Tomioka, Y., Kimura, T. & Tokura, Y. (2002). *Phys. Rev. B*, **66**, 134412.

Neubeck, W., Vettier, C., de Bergevin, F., Yakhou, F., Mannix, D., Ranno, L. & Chatterji, T. (2001). *J. Phys. Chem. Solids*, **62**, 2173–2180.

Okitsu, K., Ueji, Y., Sato, K. & Amemiya, Y. (2001). *J. Synchrotron Rad.* **8**, 33–37.

Paixão, J. A., Detlefs, C., Longfield, M., Caciuffo, R., Santini, P., Bernhoeft, N., Rebizant, J. & Lander, G. H. (2002). *Phys. Rev. Lett.* **89**, 187202.

Paolasini, L., Di Matteo, S., Deen, P. P., Wilkins, S., Mazzoli, C., Detlefs, B., Lapertot, G. & Canfield, P. (2007). *Phys. Rev. B.* Submitted.

Paolasini, L. & Lander, G. H. (2000). *J. Alloys Compd.* **303–304**, 232–238.

Paolasini, L., Vettier, C., de Bergevin, F., Yakhou, F., Mannix, D., Stunault, A., Neubeck, W., Altarelli, M., Fabrizio, M., Metcalf, P. A. & Honig, J. M. (1999). *Phys. Rev. Lett.* **82**, 4719–4722.

Scagnoli, V., Staub, U., Janoush, M., Mulders, A. M., Shi, M., Meijer, G. I., Rosenkranz, S., Wilkins, S. B., Paolasini, L. & Lovesey, S. W. (2005). *Phys. Rev. B*, **72**, 155111.

Staub, U., Meijer, G. I., Fauth, F., Allenspach, R., Bednorz, G., Karpinski, J., Kazakov, S., Paolasini, L. & d'Acapito, F. (2002). *Phys. Rev. Lett.* **88**, 126402.

Stunault, A., Soriano, S., Gourieux, T., Detlefs, C., Dufour, C. & Dumesnil, K. (2004). *J. Magn. Magn. Mater.* **272–276**, 546–548.

Stunault, A., Vettier, C., de Bergevin, F., Bernhoeft, N., Fernandez, V., Langridge, S., Lidström, E., Lorenzo-Diaz, J. E., Wermeille, D., Chabert, L. & Chagnon, R. (1998). *J. Synchrotron Rad.* **5**, 1010–1012.

Subias, G., García, J., Berau, P., Neuriva, M., Sánchez, M. C. & García Muñoz, J. C. (2006). *Phys. Rev. B*, **73**, 205107.

Vettier, C. (2001). *J. Electron. Spectrosc. Relat. Phenom.* **117–118**, 113–128.

Walker, H. C., McEwen, K. A., McMorrow, D. F., Wilkins, S. B., Wastin, F., Colineau, E. & Fort, D. (2006). *Phys. Rev. Lett.* **97**, 137203.

Wilkins, S. B., Caciuffo, R., Detlefs, C., Rebizant, J., Colineau, E., Wastin, F. & Lander, G. H. (2006). *Phys. Rev. B*, **73**, R060406.

Wilkins, S. B., Paixão, J. A., Caciuffo, R., Javorsky, P., Wastin, F., Rebizant, J., Detlefs, C., Bernhoeft, N., Santini, P. & Lander, G. H. (2004). *Phys. Rev. B*, **70**, 214402.